Materials Science & Engineering A 973 (2026) 150688

Contents lists available at ScienceDirect

Materials Science & Engineering A

journal homepage: www.elsevier.com/locate/msea

Particle morphology-dependent deformation mechanisms in sintered Cu structures

Tianxing Du [a], Chenshan Gao [b], Olof Bäcke [c], Lai Wei [a], Huaiyu Ye [b], Guoqi Zhang [a], Magnus Hörnqvist Colliander [c], Leiming Du [a,*]

[a] Department of Microelectronics, Delft University of Technology, Mekelweg 4, Delft, 2628 CD, Netherlands
[b] School of Microelectronics, Southern University of Science and Technology, Nanshan i Park Chongwen, Shenzhen, 518055, China
[c] Department of Physics, Chalmers University of Technology, Kemigården 1, Gothenburg, 412 96, Sweden

ARTICLE INFO

Keywords:
Particle morphology
Sintering
Micro-pillar compression test
Transmission Kikuchi diffraction
Molecular dynamics

ABSTRACT

Particle morphology is a critical structural variable in pressure-assisted sintering because it controls packing, pore topology, interparticle bonding and load transfer. Here, copper (Cu) was used as a model system to examine how monomodal spherical, bimodal spherical and flake-shaped particle assemblies, processed under identical conditions, form porous structures with distinct mechanical responses. Micro-pillar compression reveals low effective elastic moduli of 7.5–12.5 GPa and high yield strengths of 403–450 MPa. The deformation pathways are strongly morphology dependent. The monomodal structure accommodates strain through distributed pore collapse and particle deformation, leading to progressive densification hardening. The bimodal structure exhibits size-partitioned deformation, with large particles forming the main load-bearing backbone and smaller particles accommodating local rearrangement, embedding and shear compaction. The flake-shaped structure undergoes geometry-guided deformation, where extended face-to-face bonding enhances local load bearing, while inter-flake misalignment concentrates strain and promotes shear localization. Post-compression transmission electron microscopy (TEM) and transmission Kikuchi diffraction (TKD) analyses link these modes to pore collapse, neck deformation and grain-scale strain accommodation. TKD further gives average Geometrically Necessary Dislocations (GND) densities of 4.36×10^{14} m^{-2}, 3.69×10^{14} m^{-2} and 4.11×10^{14} m^{-2} for the monomodal, bimodal and flake-shaped structures, respectively. Molecular dynamics (MD) simulations reproduce the corresponding strain-localization patterns and reveal morphology-controlled load-transfer pathways dominated by Shockley partial dislocations. These results establish particle morphology as a design parameter for tuning stiffness, strength and damage tolerance in sintered porous metals.

1. Introduction

Sintered porous metallic particles, featuring large surface-area-to-volume ratio, low-temperature processability, and tailorable mechanical properties, have been widely applied in biomedical engineering [1–3], energy conversion and storage [4–8], catalysis [9,10], flexible electronics [11–13], and electronic packaging [14–16]. Nevertheless, the mechanical performance of sintered porous metals remains strongly constrained by the inherent porous microstructure and the associated sintered neck network [17–21]. Such microstructural features are largely dictated by particle morphology (shape and size), sintering conditions and material composition [22]. Extensive efforts have focused on optimizing sintering conditions to regulate process-structure–property-performance relationships, while parallel studies have explored diverse material compositions to further enhance mechanical performance [23,24]. However, the role of inherent particle morphology in regulating packing density and their subsequent effects on sintering dynamics and mechanical behavior remains insufficiently understood.

Monomodal spherical particles, as the most extensively adopted morphology in sintering systems, exhibit a classical neck growth mechanism dominated by surface diffusion, which facilitates the formation of stable sintered networks [25]. Under relatively mild sintering conditions, micro- and nanoscale monomodal spherical particles can achieve residual porosity below ~15%, forming continuous conductive pathways and exhibiting excellent mechanical reliability [26,27]. However, the packing limit of monomodal spherical particles, defined as the jamming density ($\phi \approx 0.64$), inherently constrains the attainable sintered density and the resulting mechanical strength of the particle

* Corresponding author.
E-mail address: L.Du@tudelft.nl (L. Du).

https://doi.org/10.1016/j.msea.2026.150688
Received 18 May 2026; Received in revised form 19 June 2026; Accepted 29 June 2026
Available online 9 July 2026

network [28]. To alleviate these constraints, bimodal spherical particles systems have been introduced as a hierarchical packing strategy, enabling a higher jamming density of more than 0.70 through interstitial filling effects, which in turn promotes enhanced densification behavior and improved mechanical performance [29]. For example, Wang et al. [30] demonstrated that bimodal particles enable nanoparticles (NPs) to occupy intragranular and interfacial regions, leading to grain refinement and more uniform plastic deformation, thereby facilitating a synergistic enhancement of strength and ductility. Although interparticle necks between spherical particles provide structural continuity, insufficient neck growth can restrict load-transfer efficiency and thereby limit the mechanical performance of the sintered network. Accordingly, non-spherical particles, including nanowires and flakes, have been incorporated to establish bridging pathways, thereby facilitating load redistribution and improving deformation capacity [31–33]. For example, Chen et al. [34] observed enhanced strength in flake-shaped structures and attributed this improvement to a significantly increased neck-growth ratio (~0.67 compared to ~0.38 for spherical particles), enabling more continuous interparticle bonding and more efficient load-transfer pathways within the sintered network.

Conventionally, plastic deformation in bulk metals is primarily accommodated by dislocation activities, while grain boundaries (GBs) regulate dislocation accumulation or movement and may additionally trigger twinning or other boundary mediated processes, collectively shaping the mechanical response [35–38]. Specifically, plastic deformation of single-crystal copper (Cu) is predominantly governed by the glide motion of dislocations, where orientation-dependent slip activity and dislocation dissociation processes control strain accommodation and deformation anisotropy [39]. In polycrystalline metals, plasticity is strongly governed by grain-grain interactions and intergranular constraints, leading to heterogeneous deformation characterized by orientation gradients and defect accumulation, which collectively shape the macroscopic mechanical response [40,41]. As the structural length scale is further refined toward the nanograined regime, the role of microstructural interfaces becomes increasingly dominant, giving rise to a transition from compatibility driven deformation toward plasticity mediated by GBs. In this regime, the classical Hall-Petch paradigm may deviate, and grain boundary (GB) stability emerges as a critical factor governing deformation mechanisms and hardness [42]. Furthermore, gradient nano-grained structures leverage spatial variations in microstructural length scale to redistribute strain and suppress localization, where plastic deformation is accommodated by mechanically driven GB migration and concomitant grain growth, enabling an unusual combination of high strength and large tensile plasticity [43]. Copper alloys further broaden this structure–property relationship by showing that heterophase interfaces, rather than grain boundaries alone, can regulate deformation and functional performance [44]. For example, Fu et al. recently reported a lead-free graphite-brass in which in situ formed lamellar TiC bridges graphite and the BCC β phase, anchoring graphite within the Cu–Zn matrix and improving machinability, hardness and electrical conductivity [45]. However, sintered porous systems are compliant, geometry-sensitive load-bearing networks, in which microstructural heterogeneity substantially complicates deformation and structural evolution [46–49]. Under such conditions, plasticity is no longer governed solely by GBs but emerges from the coupled interplay of interfacial diffusion, load redistribution, and localized structural reconfiguration [50,51]. Given that particle morphology governs pore structure, interparticle connectivity, and load-transfer pathways, elucidating its influence on mechanical properties is essential for understanding deformation mechanisms in sintered porous systems.

In this work, three representative particle morphologies, including monomodal, bimodal, and flake-shaped particles, were selected as model systems, and their mechanical responses were systematically characterized via micro-pillar compression tests. Post-deformation microstructure characterization was examined through scanning electron microscopy (SEM), transmission electron microscopy (TEM), and transmission Kikuchi diffraction (TKD). Moreover, molecular dynamics (MD) simulations were performed to reveal the atomistic-level mechanisms underlying structural evolution during sintering and subsequent compression. Through the synergistic integration of experiments and simulations, this work establishes a comprehensive understanding of the intrinsic correlations between particle morphology-dependent microstructure evolution and the resulting mechanical behaviors.

2. Experimental and simulation method

2.1. Sample preparation

Figs. 1a–c present the initial SEM morphologies of three types of Cu particles, namely monomodal, bimodal, and flake-shaped particles. All Cu powders had a nominal purity of 99.99%, meeting the purity requirement for industrial electronic-packaging pastes [52]. The monomodal powder consisted of spherical Cu nanoparticles with an average diameter of approximately 150 nm. The bimodal powder contained small spherical particles with a diameter of approximately 150 nm and large spherical particles with a diameter of approximately 1.5 μm, which provides a highly asymmetric bimodal packing that facilitates interstitial filling by smaller particles [53]. The flake-shaped powder exhibited a disk-shaped morphology, with a lateral diameter of approximately 2–7.5 μm and an aspect ratio of about 3:1 to 15:1. The final paste contained 77 wt% Cu particles and an organic vehicle composed of ethylene glycol and terpineol at a mass ratio of 1:1. A pressure-assisted sintering process was employed to fabricate the sintered Cu samples (Fig. 1d). Cu paste was screen-printed onto a Cu substrate and preconditioned at 120 °C for 5 min under a nitrogen atmosphere to remove residual solvents. An aluminum (Al) film was applied as a temporary capping layer. Pressure-assisted sintering was conducted at 250 °C under a uniaxial pressure of 30 MPa for 5 min in a reducing atmosphere (5% H_2/N_2). After cooling to room temperature, the Al film was removed to expose the sintered Cu layer. The porosity after sintering was estimated from representative cross-sectional SEM images. The corresponding pore fractions were approximately 8%, 11% and 22% for the monomodal, bimodal and flake-shaped particle systems, respectively (Fig. S1). Micro-pillars for compression tests were then fabricated by focused ion beam (FIB) milling using a dual-beam FEI Helios G4 CX FIB-SEM system (Fig. 1e). The fabricated micro-pillars had a diameter of approximately 5 μm and a height of about 12.5 μm, corresponding to an aspect ratio of ~2.5:1. This geometry effectively suppresses buckling instability and ensures sufficient mechanical stability during subsequent compression tests [54].

2.2. Micro-pillar compression tests

Mechanical tests were performed using an Alemnis in situ nanoindentation system (Alemnis AG, Switzerland) integrated within a Zeiss Ultra55 SEM. Uniaxial compression was carried out with a flat-punch diamond tip (nominal radius: 10 μm) under displacement control at a loading rate of $10\,nm\,s^{-1}$, as schematically illustrated in Fig. 1f. Prior to testing, the specimens were carefully leveled and aligned to ensure axial loading and to minimize bending or eccentric effects. A small preload was applied to establish stable contact and reduce the influence of surface irregularities. Representative micro-pillars fabricated from the monomodal, bimodal and flake-shaped structures are shown in Figs. 1g–i, respectively. Load–displacement data were continuously recorded throughout the experiments. For statistical reliability, four independent micro-pillars were tested for each particle morphology under identical conditions. Post-compression analysis was conducted to characterize the deformation behavior of the sintered Cu, with particular emphasis on yield behavior, strain hardening and failure mechanisms [55].

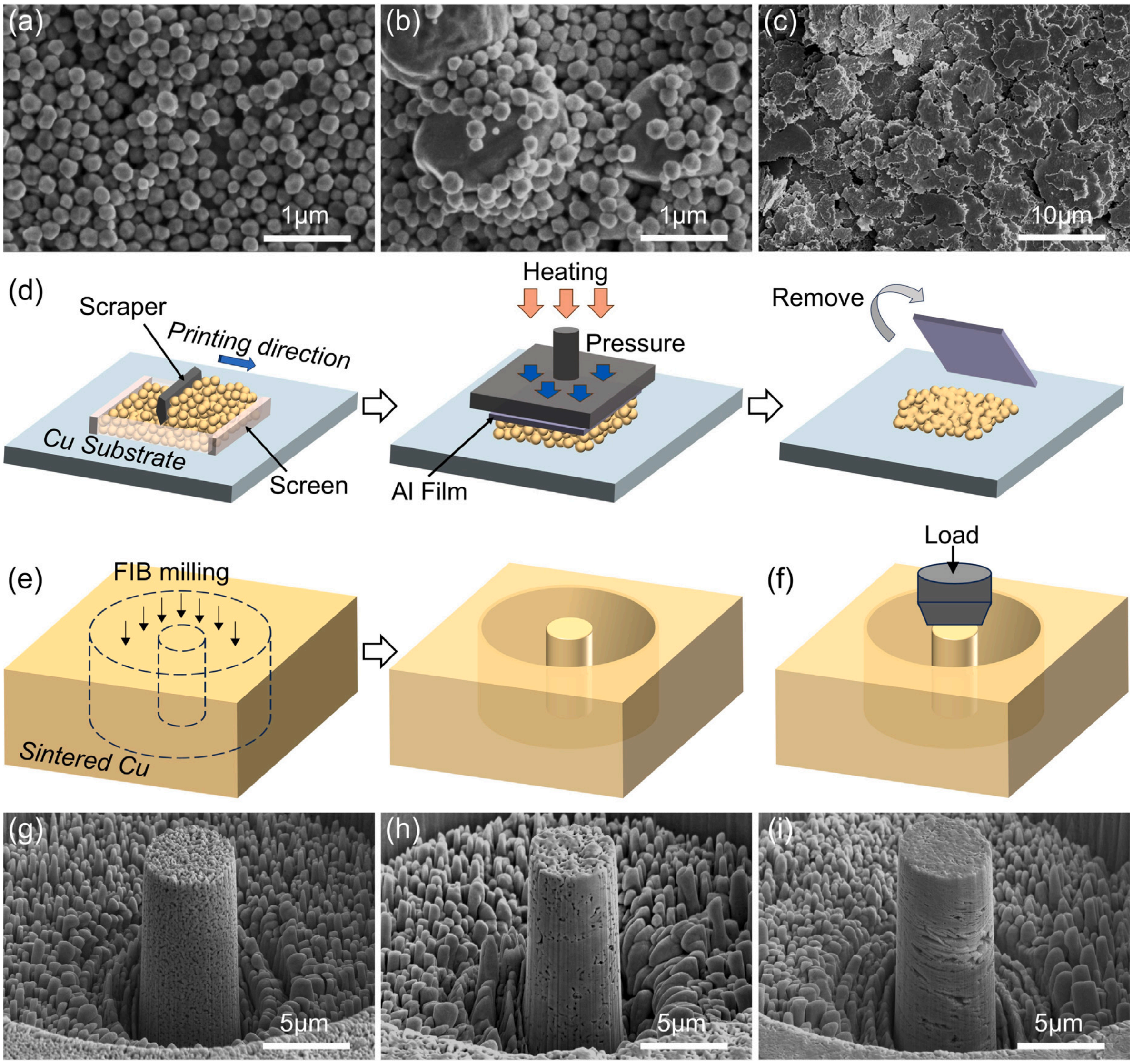

Fig. 1. Experimental workflow for preparing and compressing sintered Cu micro-pillars with different particle morphologies. (a–c) SEM images of the monomodal spherical, bimodal spherical, and flake-shaped Cu particles. (d) Stencil printing of Cu paste on a Cu substrate followed by pressure-assisted sintering with a temporary Al film, heating, applied pressure, and subsequent Al film removal. (e) FIB fabrication of cylindrical micro-pillars from the sintered Cu layer. (f) In situ flat-punch compression testing. (g–i) Representative SEM images of fabricated micro-pillars with monomodal, bimodal, and flake-shaped structures, respectively.

2.3. TEM and TKD characterization

The microstructure evolution of sintered Cu particle micro-pillars before and after mechanical deformation was systematically characterized using TEM and TKD. TEM observations were performed on FIB-milled lamellae with a final thickness of approximately 100 nm using a Cs-corrected Titan Themis microscope to directly resolve particle morphology, sintering necks, dislocation structures, and deformation-induced defects within the sintered network, thereby providing insight into nanoscale deformation mechanisms. TKD analyses were conducted using Hitachi Regulus 8230 SEM at an accelerating voltage of 30 kV and a scanning step size of 5 nm. Compared with conventional electron backscatter diffraction (EBSD), TKD offers substantially higher spatial resolution (<10 nm), enabling reliable characterization of nanocrystalline grain orientations and GB evolution, which is essential for elucidating crystallographic deformation mechanisms. [56,57].

2.4. MD simulation

MD simulations were performed using the Large-scale Atomic/Molecular Massively Parallel Simulator (LAMMPS) [58] to investigate the influence of particle morphology on the sintering process and subsequent mechanical response. Atomic configurations, dislocation activity, and local crystal structure during sintering and deformation were analyzed using the Open Visualization Tool (OVITO) [59]. Interatomic interactions were described by the embedded-atom method (EAM) potential developed by Williams et al. [60], which has been extensively validated for simulations involving lattice defects, diffusion phenomena, and mechanical deformation in Cu systems.

To elucidate morphology-dependent microstructure evolution during sintering, three representative particle models were constructed, with key parameters summarized in Table 1. The monomodal and bimodal particle models were generated under fully periodic boundary conditions to approximate bulk-like packing environments. In contrast,

Table 1
Summary of model construction parameters.

Parameter	Monomodal particles model	Bimodal particles model	Flake-shaped particles model
Simulation domain	300 Å × 300 Å × 1250 Å	300 Å × 300 Å × 1250 Å	300 Å × 300 Å × 1550 Å
Boundary condition	Fully periodic (x, y, z)	Fully periodic (x, y, z)	Periodic (x, y); non-periodic (z) with ±100 Å free space at top and bottom
Particle morphology	Monomodal spherical particles	Bimodal spherical particles	Disk-shaped flake particles
Particle size	Diameter: 40 Å (σ = 20 Å)	Large spheres: 200 Å + small spheres: 40 Å (σ = 20 Å)	Diameter: 290 Å; thickness: 20 Å
Orientation assignment	Random crystallographic orientation	Random crystallographic orientation	Voronoi-based random polycrystallinity
Model size	~3.5 million atoms	~4.0 million atoms	~4.0 million atoms

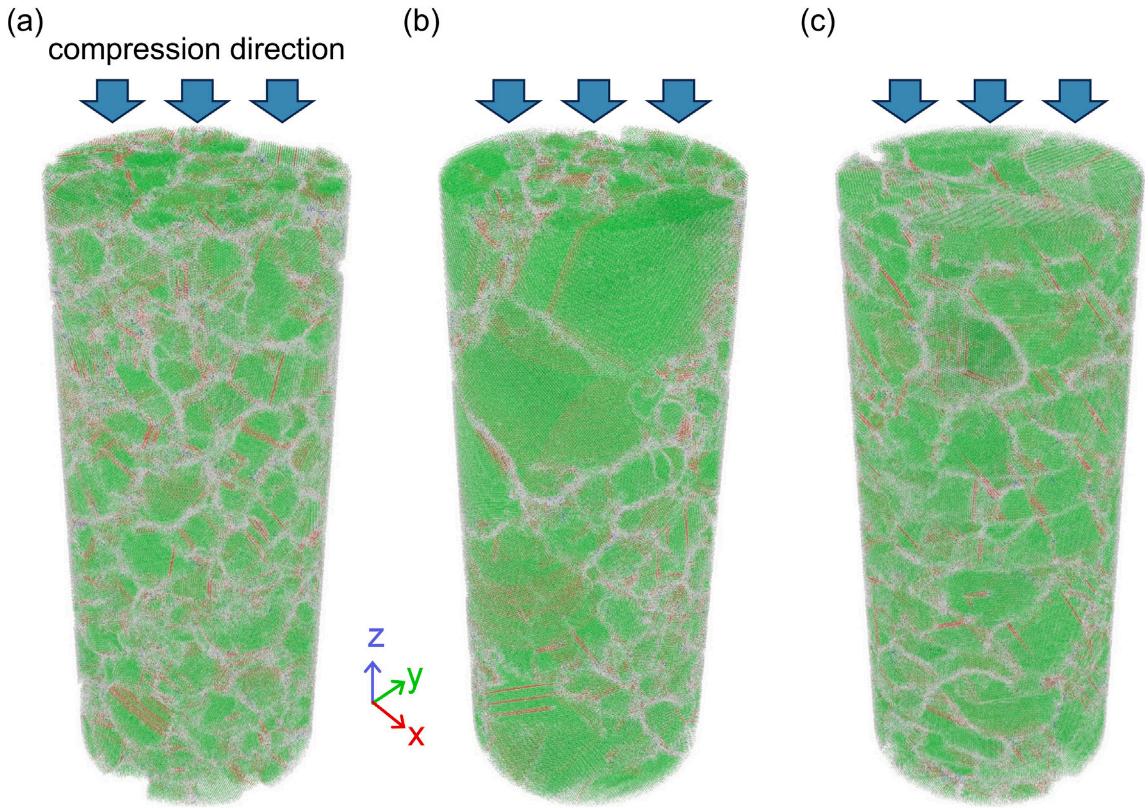

Fig. 2. Pre-compression atomistic Cu micro-pillar models used for MD simulations. (a–c) Monomodal, bimodal, and flake-shaped particle-derived models after simulated sintering and cylindrical trimming, respectively.

the flake-shaped particle model employed periodic boundaries in the in-plane directions and a non-periodic boundary along the z direction, with an additional 100 Å free space introduced above and below the stacked structure to permit structural relaxation normal to the stacking direction. The monomodal spherical particle model was generated by random packing of spherical particles with normally distributed diameters and independent crystallographic orientations. Based on this configuration, the bimodal spherical particle model incorporated hierarchical packing by inserting larger spheres prior to the introduction of smaller particles, thereby enhancing microstructural heterogeneity. The flake-shaped particle model was constructed using a layer-by-layer assembly approach, in which disk-shaped crystalline flakes with Voronoi-defined grain structures were sequentially stacked. To represent slight stacking misalignment in practical flake-powder assemblies while retaining nanoscale inter-flake gaps for diffusion-driven neck formation, the flakes were initialized with an inter-flake spacing of 10 Å, an in-plane tilt of 3.5°, and independent lateral misalignments within ±100 Å. Following assembly, global overlap removal was applied to eliminate atomic interpenetration, resulting in final models containing approximately 3.5–4.0 million atoms. The corresponding initial particle packing configurations of the monomodal, bimodal, and flake-shaped models are shown in Figs. S2a1–c1, respectively.

The sintering process was simulated using a three-step protocol. The system was first heated from 300 K to 523 K over 100 ps under an isotropic NPT ensemble with a Nosé–Hoover thermostat to promote atomic diffusion and sintering neck formation. Subsequently, a uniaxial compressive strain of 40% was applied along the z direction to emulate pressure-assisted densification at a strain rate of 1×10^9 s^{-1}. The system was then equilibrated at 523 K for 100 ps to relax residual stresses induced by the high strain rate [61]. The sintered configurations of the three particle models are shown in Figs. S2a2–c2.

Following sintering, the configurations were trimmed into cylindrical pillars with a maximum height of 750 Å. Periodicity was retained along the z direction to approximate axial deformation, whereas the x and y directions were treated as non-periodic to eliminate lateral periodic interactions during micro-pillar compression. The resulting pillars

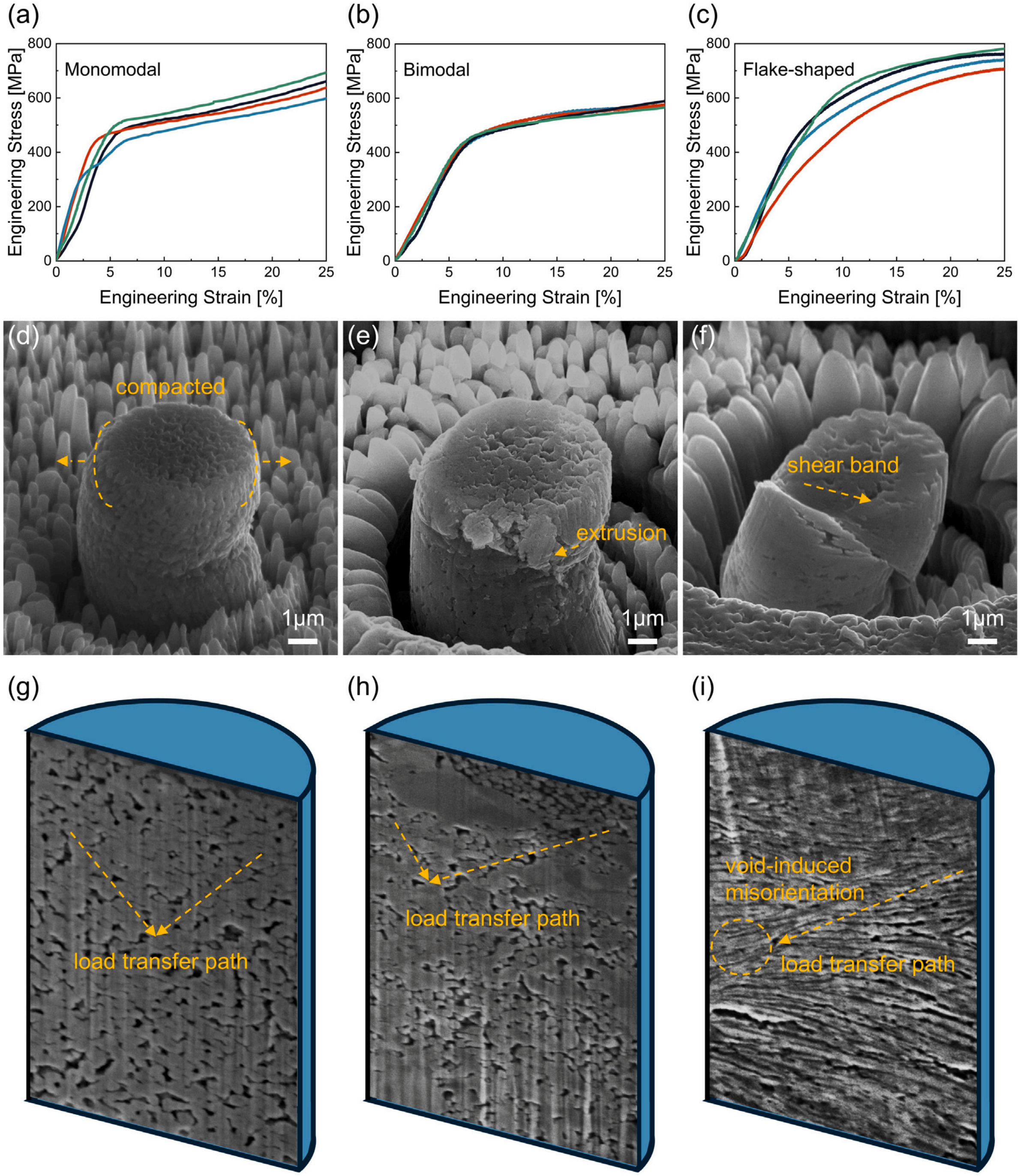

Fig. 3. Morphology-dependent mechanical response and deformation modes of sintered Cu micro-pillars. (a–c) Engineering stress–strain curves from micro-pillar compression tests of monomodal, bimodal, and flake-shaped structures, respectively. (d–f) Post-compression SEM images showing morphology-dependent deformation, including relatively axisymmetric compaction in the monomodal pillar, extrusion in the bimodal pillar, and shear-band-like deformation in the flake-shaped pillar. (g–i) Schematic cross-sectional interpretations of the corresponding load-transfer paths and deformation modes.

exhibited an aspect ratio of approximately 2.5:1, comparable to experimental compression specimens. The corresponding pre-compression configurations of the monomodal, bimodal, and flake-shaped particle models are shown in Figs. 2a–c. Prior to compression, the system was energy-minimized and equilibrated at 300 K under an NVT ensemble for 20 ps. Compression was then applied along the z direction at a constant engineering strain rate of 1×10^9 s^{-1} until a total compressive strain of ~40% was reached, while maintaining the temperature at 300 K. After deformation, the system was further relaxed at 300 K for 50 ps to allow stress redistribution and structural equilibration.

3. Results and discussion

3.1. Mechanical properties

Figs. 3a–c present the stress–strain curves obtained from micro-pillar compression tests. The monomodal and bimodal structures exhibit a clear increase in flow stress after yielding, consistent with densification-induced hardening. In contrast, the flake-shaped structure shows no sharply defined yield point; instead, the stress increases gradually with strain, indicating a progressive transition from elastic to plastic deformation, with partial overlap between the two regimes

Table 2
Summary of mechanical properties of different particle morphologies.

Property	Monomodal particles	Bimodal particles	Flake-shaped particles
Elastic modulus, E (GPa)	12.53 ± 0.72	7.43 ± 0.27	7.84 ± 0.85
Yield strength, σ_y (MPa)	403.01 ± 36.46	434.11 ± 9.54	450.65 ± 65.84

during compression [62]. This behavior can be attributed to the concurrent occurrence of progressive pore collapse and compaction of misaligned inter-flake regions. The corresponding mechanical properties are summarized in Table 2. The elastic modulus was extracted from the initial linear portion of the stress–strain curve, whereas the yield strength was determined using the 0.2% offset criterion [63]. The monomodal structure shows the highest modulus, 12.53 ± 0.72 GPa, followed by the bimodal and flake-shaped structures, with values of 7.43 ± 0.27 and 7.84 ± 0.85 GPa, respectively. In contrast, the yield strength increases from 403.01 ± 36.46 MPa for the monomodal structure to 434.11 ± 9.54 MPa for the bimodal structure and 450.65 ± 65.84 MPa for the flake-shaped structure. These values are consistent with the reported modulus and strength ranges of pressure-assisted sintered Cu specimens, supporting the reliability of the measured mechanical response [17,47,51]. Notably, the yield strengths of all three sintered structures fall within the intermediate-to-high strength regime of Cu. They are higher than single-crystalline and bicrystalline Cu micro-pillars (~40–280 MPa) [64–67], and are comparable to polycrystalline Cu micro-pillars (~250–400 MPa) [68–70], while remaining below the strength levels typically achieved in nanocrystalline Cu pillars (~400–900 MPa) [71–73]. In contrast, their elastic moduli (~7–15 GPa) are substantially lower than that of bulk Cu (~50–110 GPa) [74–76]. This combination of high yield strength and low elastic modulus mainly originates from the discrete load-bearing nature of the porous sintered structure.

To rationalize the morphology-dependent variations in modulus and strength, Figs. 3d–i compare the post-compression pillar morphologies and corresponding cross-sectional deformation features. For the monomodal structure, the compressed pillar retains a relatively smooth and nearly axisymmetric profile (Fig. 3d). The cross-section shows a comparatively uniform distribution of pores and sintered necks (Fig. 3g), indicating that the applied load is transferred through a relatively homogeneous particle skeleton. This topology promotes uniform compaction along the loading direction, with the monomodal particles undergoing relatively homogeneous deformation and distributed pore collapse as schematically illustrated in Fig. S3a. The resulting deformation mode is similar to the axisymmetric plastic flow reported for single-crystalline Cu micro-pillars [77]. The bimodal structure shows a more heterogeneous deformation morphology after compression (Fig. 3e), where pronounced extrusion is observed. Although bimodal packing is generally expected to increase the packing density relative to monomodal packing [78,79], the measured elastic modulus is lower. This can be attributed to the pronounced microscale heterogeneity introduced by the coexistence of large and small particles [80], which interrupts continuous load transfer and reduces the effective stiffness of the load-bearing network. In the cross-section, deformation is no longer uniformly distributed but is concentrated around large-particle regions (Fig. 3h), with large particles forming the primary load-bearing framework (Fig. S3b). The additional interfaces associated with the fine particles may facilitate local stress redistribution and delay macroscopic yielding [81], giving rise to the higher yield strength of the bimodal structure. With further compression, however, load transfer becomes increasingly dominated by particle-scale paths through the coarse-particle framework. Once these regions exceed their local bearing capacity, deformation localizes and lateral material flow develops, producing the observed extrusion features. The flake-shaped structure exhibits the most anisotropic deformation response (Fig. 3f). Its relatively low elastic modulus is associated with the high compliance of the platelet network during the early loading stage. The packing of plate-like particles promotes jamming and internal void formation, allowing local pore collapse and structural rearrangement at small strains [82]. Because platelet rotation is constrained by geometric anisotropy and interlocking, deformation proceeds mainly through progressive flattening, stack compaction and local rearrangement rather than free particle rotation as illustrated in Fig. S3c [83]. The cross-section further reveals pronounced shear localization associated with misoriented platelet domains and void-rich regions (Fig. 3i). Collapse of these regions introduces local incompatibility between adjacent flake blocks, deflects the load-transfer path and promotes shear-band formation. Despite its reduced stiffness, the flake-shaped structure exhibits the highest yield strength. This strength increase is attributed to extended face-to-face platelet contacts, which form strongly bonded block-like domains, and to geometric interlocking that resists sliding and structural instability under axial compression [84]. Thus, deformation evolves from compliant compaction at small strain to shear-dominated localization at larger strain, while the interlocked platelet network sustains higher applied stresses before yielding.

3.2. TEM analysis

To elucidate the underlying deformation mechanisms, TEM characterization was conducted on compressed micro-pillars with the three particle structures (Figs. 4, 5). The TEM lamella preparation procedure and sampling positions are shown in Fig. S4. For the monomodal structure, the initially equiaxed particles are progressively flattened after compression, with the most severe deformation located near the central region of the pillar (Fig. 4a). This region shows pronounced grain distortion and reduced porosity, indicating that plastic deformation is closely coupled with structural densification (Fig. 4c). The deformation is therefore governed by the combined effects of dislocation-mediated plasticity, pore collapse, and mechanical constraint from interparticle necks. In highly strained regions, continued pore shrinkage indicates densification assisted by dislocation activity and particle accommodation (Fig. 4d). However, residual pores remain even after substantial deformation, reflecting the limitation of the sintered structure, where incomplete interparticle bonding prevents full densification. These pores introduce local compliance variations and promote preferential deformation in mechanically softer regions, rather than a uniform strain field throughout the pillar. This behavior differs from the continuous dislocation-mediated plastic flow in fully dense Cu, where strain is accommodated within an uninterrupted crystalline lattice instead of being controlled by pore-induced compliance heterogeneity [85].

The bimodal structure exhibits much stronger strain localization, directly associated with its heterogeneous particle arrangement (Fig. 4b). Deformation is mainly concentrated in regions dominated by large particles, which form the primary load-bearing backbone. Although the resulting localization is macroscopically reminiscent of shear localization in metallic glasses, its origin here lies in interfacial stress gradients generated by microstructural heterogeneity [86]. In highly strained regions, cracks initiate along the surfaces of large-particle platforms (Fig. 4e), corresponding to insufficiently sintered regions arising from particle shadowing effects [87]. Under compression, small particles in these regions rotate, slide, and spread laterally, producing intense localized plastic flow. The incompatibility between axial compression and lateral material flow generates tensile and shear components along large-particle interfaces, thereby promoting crack initiation and propagation. This behavior is analogous to fracture in porous ceramics under compression, where structural heterogeneity produces local stress concentration and localized failure [88]. Meanwhile, small particles

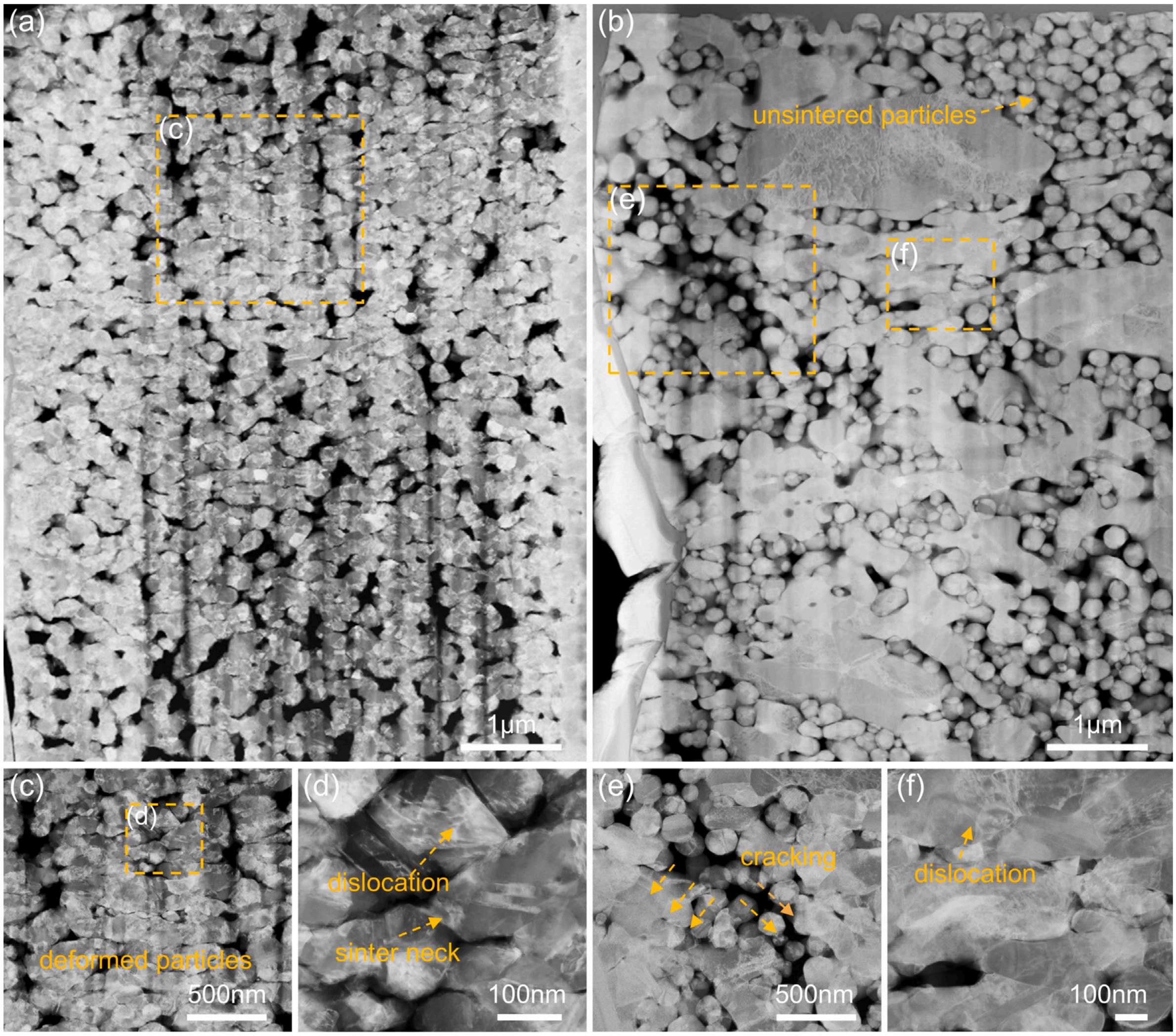

Fig. 4. TEM characterization of compressed monomodal and bimodal sintered Cu micro-pillars. (a, b) Low-magnification TEM overviews of the monomodal and bimodal pillars after compression, respectively. (c–f) High-magnification HAADF-STEM images providing clearer evidence of local deformation features. (c) Primary deformation zone in the monomodal structure. (d) Local deformation details in the monomodal structure, showing dislocation-related contrast and sintering-neck deformation. (e) Extrusion-induced cracking in the bimodal structure. (f) Highly strained region in the bimodal structure, showing dislocation-related contrast.

located at interparticle boundaries undergo severe shear and compressive deformation, leading to localized densification and rearrangement (Fig. 4f). Thus, the deformation of the bimodal structure is governed by force-chain-mediated strain partitioning, interfacial incompatibility, and particle-scale plastic accommodation.

The flake-shaped structure deforms through a mechanism governed by morphology-induced anisotropy, which produces highly aligned lamellar domains and locally misaligned interdomain regions (Fig. 5a). In the aligned regions, face-to-face contacts between platelets form compact lamellar units that accommodate compression mainly through densification and dislocation-mediated plasticity (Fig. 5b). By contrast, regions containing misaligned platelets act as preferential sites for strain incompatibility and shear accommodation (Fig. 5c). The associated deformation is accompanied by dislocation accumulation, platelet bending/fracture, and the retention of uncompacted voids, indicating that local densification is incomplete even within severely deformed regions (Fig. 5d). Local bending of platelets in these regions generates tensile opening stresses at weakly bonded interfaces, leading to crack initiation along the platelet boundaries (Fig. 5e). Similar cracking associated with deformation incompatibility has been reported in freeze-cast lamellar materials, although in those systems it is often linked to buckling or fracture of continuous lamellae [89]. Thus, deformation in the flake-shaped structure is controlled by the competition between compaction of aligned platelet stacks and instability at misaligned, void-containing inter-domain regions.

3.3. TKD analysis

To clarify the role of particle morphology in grain-scale deformation during compression, TKD was performed on TEM lamellae prepared from the corresponding structures before and after deformation. The Inverse Pole Figure (IPF) map of the compressed monomodal structure reveals a relatively uniform fine-grained microstructure, with an average grain size of ~100 nm and a mean aspect ratio of ~1.74 (Fig. 6a). Compared with the original microstructure (Fig. S5a), the grains in compressed samples exhibit deformation-induced shape changes but retain a largely random crystallographic orientation distribution, without discernible strain localization or a pronounced preferred texture. This indicates that the monomodal structure accommodates compression through relatively homogeneous grain-scale deformation [90]. By contrast, incorporating larger grains produces a more heterogeneous deformation morphology in the bimodal structure (Fig. 6d). The mean aspect ratio of these grains increases markedly from 1.91 (Fig. S5d) before compression to nearly 5 after compression, together

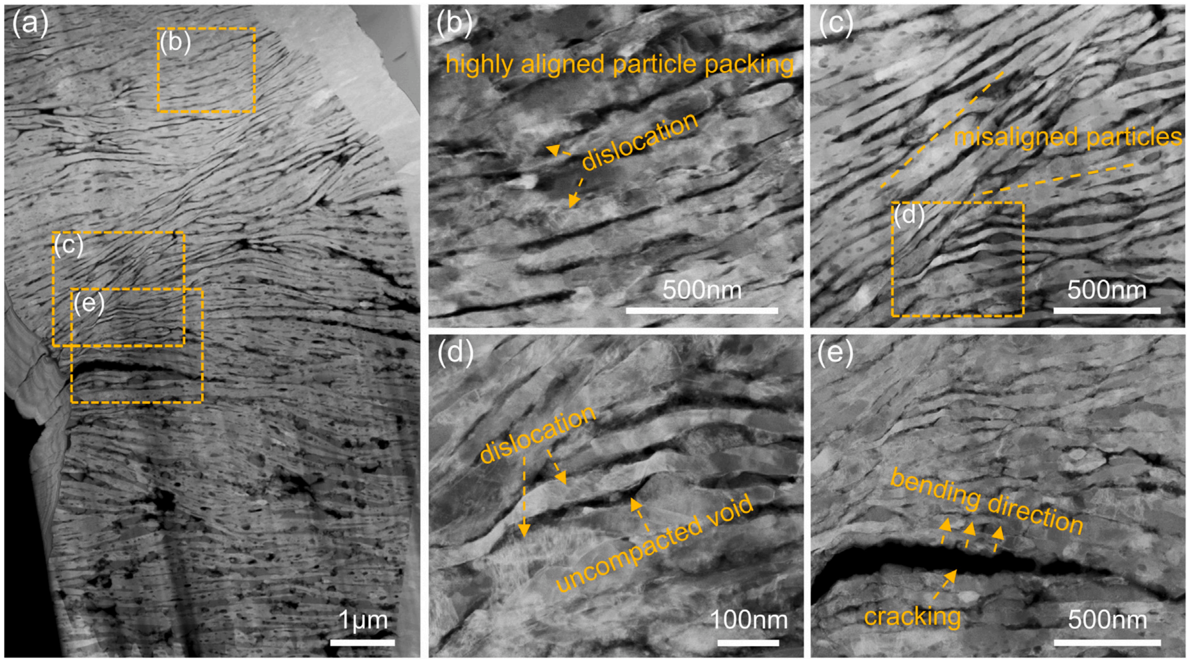

Fig. 5. TEM characterization of the compressed flake-shaped sintered Cu micro-pillar. (a) Low-magnification overview after compression. (b) Highly aligned lamellar region formed by parallel sintered flakes. (c) Misaligned interfacial regions between flake-derived domains. (d) Highly deformed region showing local dislocation activity and an uncompacted void. (e) Bending-induced cracking region.

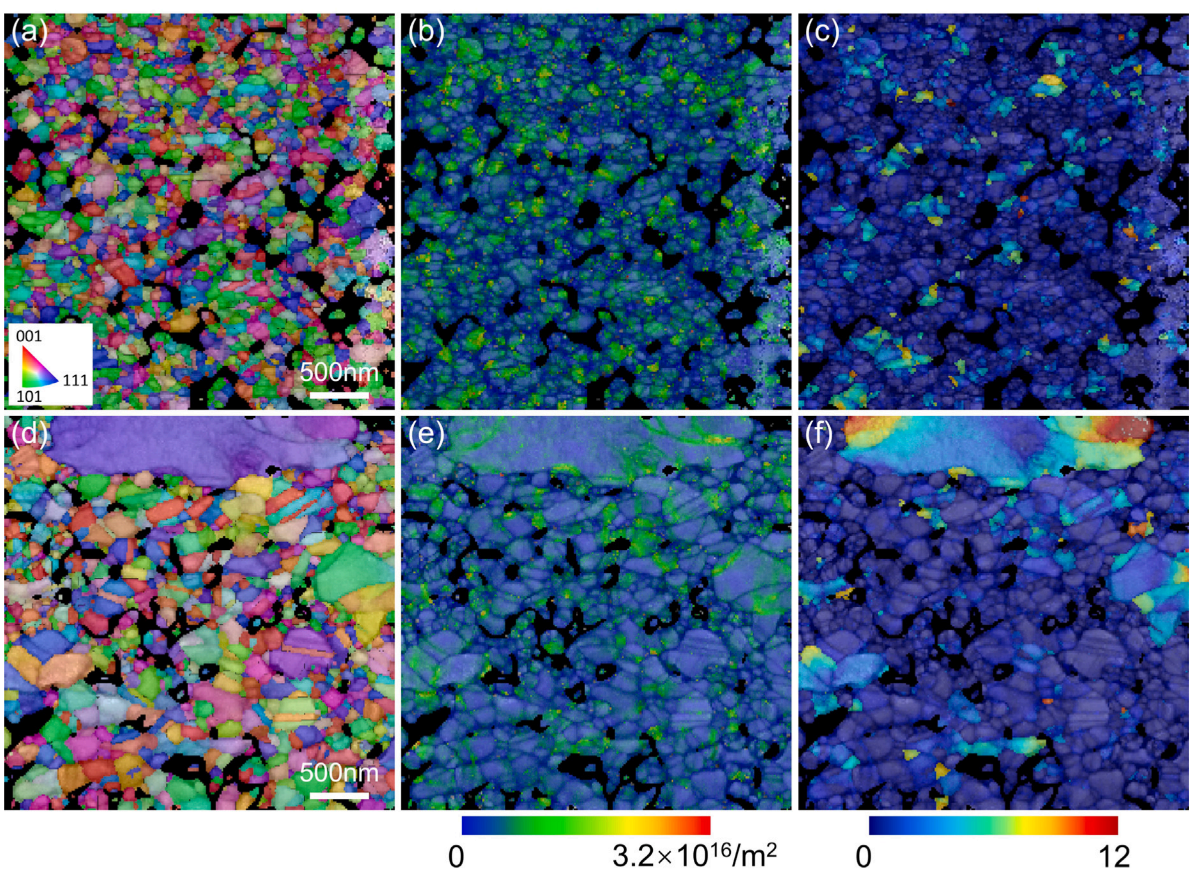

Fig. 6. TKD analysis of compressed monomodal and bimodal sintered Cu structures. (a–c) IPF map, GND density map, and GROD map of the monomodal structure, respectively. (d–f) Corresponding IPF, GND density, and GROD maps of the bimodal structure.

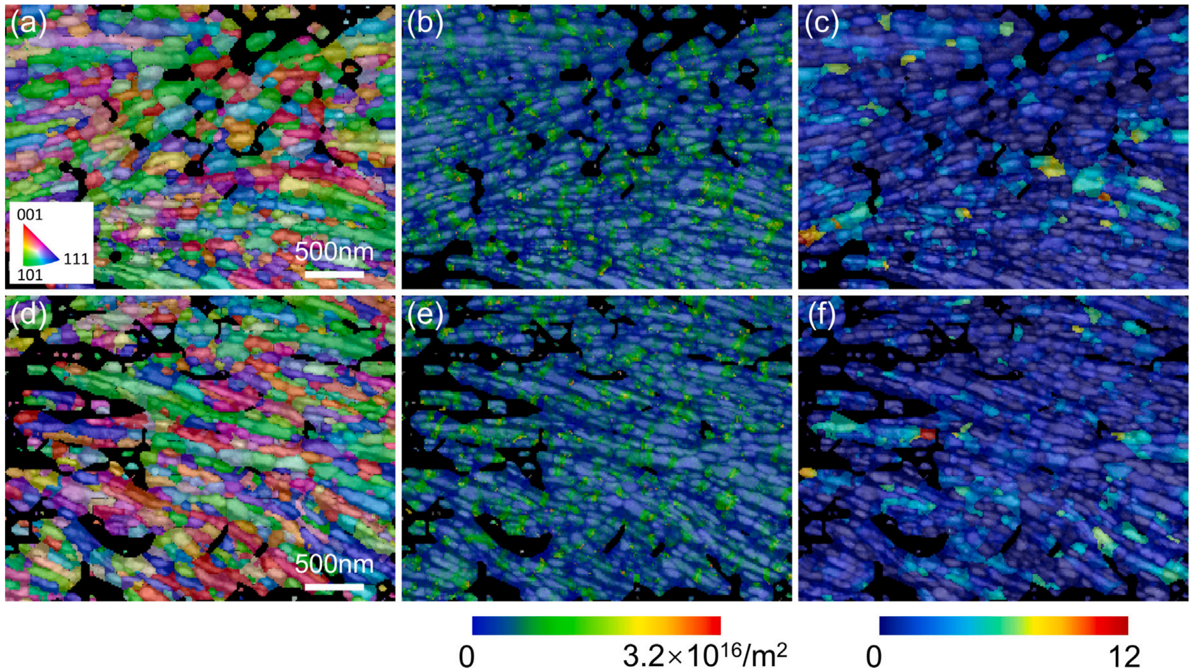

Fig. 7. TKD analysis of localized deformation in the compressed flake-shaped sintered Cu structure. (a–c) IPF, GND density, and GROD maps of a misaligned region, respectively. (d–f) Corresponding IPF, GND density, and GROD maps of a cracking region.

with the development of intragranular deformation twins. These features indicate that the large-grain constituent serves as the primary load-bearing framework during compression. The Geometrically Necessary Dislocations (GND) density map shows a broadly uniform increase in dislocation storage in the compressed monomodal structure (Fig. 6b). The average GND density increases from 2.59×10^{14} m^{-2} in the original microstructure (Fig. S5b) to 4.36×10^{14} m^{-2} after compression, without pronounced spatial localization. The Grain Reference Orientation Deviation (GROD) map, which reflects grain-scale lattice rotation and intragranular orientation gradients, further shows an increase in the average value from 0.66 to 1.14 after compression (Fig. 6c and Fig. S5c). Notably, regions with elevated GROD are arranged along a relatively symmetric load-transfer path rather than forming isolated deformation bands. The combination of a nearly uniform GND field and an axisymmetrically organized GROD distribution therefore indicates that plastic accommodation in the monomodal structure is spatially distributed but mechanically coordinated, consistent with axisymmetric deformation of the fine-grained skeleton under compression [91]. In contrast to the relatively uniform GND field in the monomodal structure, the bimodal structure exhibits a more spatially localized dislocation distribution after compression (Fig. 6e). The average GND density increases from 2.26×10^{14} to 3.69×10^{14} m^{-2} (Fig. S5e), with the accumulated dislocations preferentially concentrated at coarse/fine particle transition regions and within the interiors of the larger grains. This heterogeneous GND distribution indicates that the fine-particle matrix, owing to its higher interfacial density and stronger geometrical constraint, acts as a pinning sites for dislocations that restricts slip transfer, whereas the larger grains provide longer effective slip distances and therefore accommodate a larger fraction of plastic deformation [92]. The GROD map further reinforces this localized deformation characteristic as shown in Fig. 6f. The average GROD value increases from 1.14 (Fig. S5f) before compression to 1.51 after compression, and the higher GROD regions are preferentially located within the larger grains. This spatial correspondence between high GROD and large-grain domains indicates that the larger grains undergo more pronounced intragranular orientation deviation and lattice rotation, further supporting their dominant role in plastic deformation accommodation [93]. The cooperative interaction between constrained fine particles and more deformable large grains regulates the compression process and promotes preferential deformation of the large-grain framework, which is consistent with the observed extrusion of the larger particles.

Compared with the spherical-particle structures, the flake-shaped structure exhibits a more anisotropic compression response, governed by the inherited high-aspect-ratio platelet morphology. The IPF map shows that the dominant grain domains have an average length of ~700 nm and a thickness of ~220 nm, confirming a pronounced platelet-like geometry (Fig. 7a). After compression, the mean grain aspect ratio decreases from 3.9 in the original microstructure (Fig. S5g) to ~3.0, which is attributed to bending and fragmentation of misaligned flakes that subdivide the originally elongated grain domains. In the crack region, pronounced grain tortuosity and bending are observed above the crack, whereas grains on the right side remain relatively parallel and compacted (Fig. 7d). This spatial contrast suggests that block-like misalignment and inter-flake discontinuity facilitate crack initiation or propagation in the flake-shaped structure [94]. The GND density maps further reveal the strain-gradient response associated with compression of the flake-shaped structure (Figs. 7b, e). In contrast to the spatially distributed GND field in the monomodal structure and the locally partitioned GND accumulation in the bimodal structure, the flake-shaped structure develops directionally continuous GND-enriched bands across relatively large flake domains [95]. Their quasi-vertical continuity, approximately parallel to the compression direction, indicates that plastic strain gradients are organized along morphology-defined load-bearing paths. Compared with the original microstructure, the average GND density increases from 3.28×10^{14} to 4.11×10^{14} m^{-2} (Fig. S5h). More importantly, the dominant GND accumulation evolves from localized regions near flake junctions into chain-like bands extending along the compression direction. This transition indicates that compression amplifies pre-existing morphology-controlled strain-gradient pathways and converts local inter-flake constraints into a more continuous load-bearing network. Unlike the spherical-particle structures, the flake-shaped structure exhibits a reduction in average GROD after compression, from 3.08 in the original microstructure (Fig. S5i) to 2.52 after deformation (Figs. 7c, f). This decrease should not be interpreted as reduced plastic activity, but rather as a change in the dominant deformation mode. Owing to the extended face-to-face

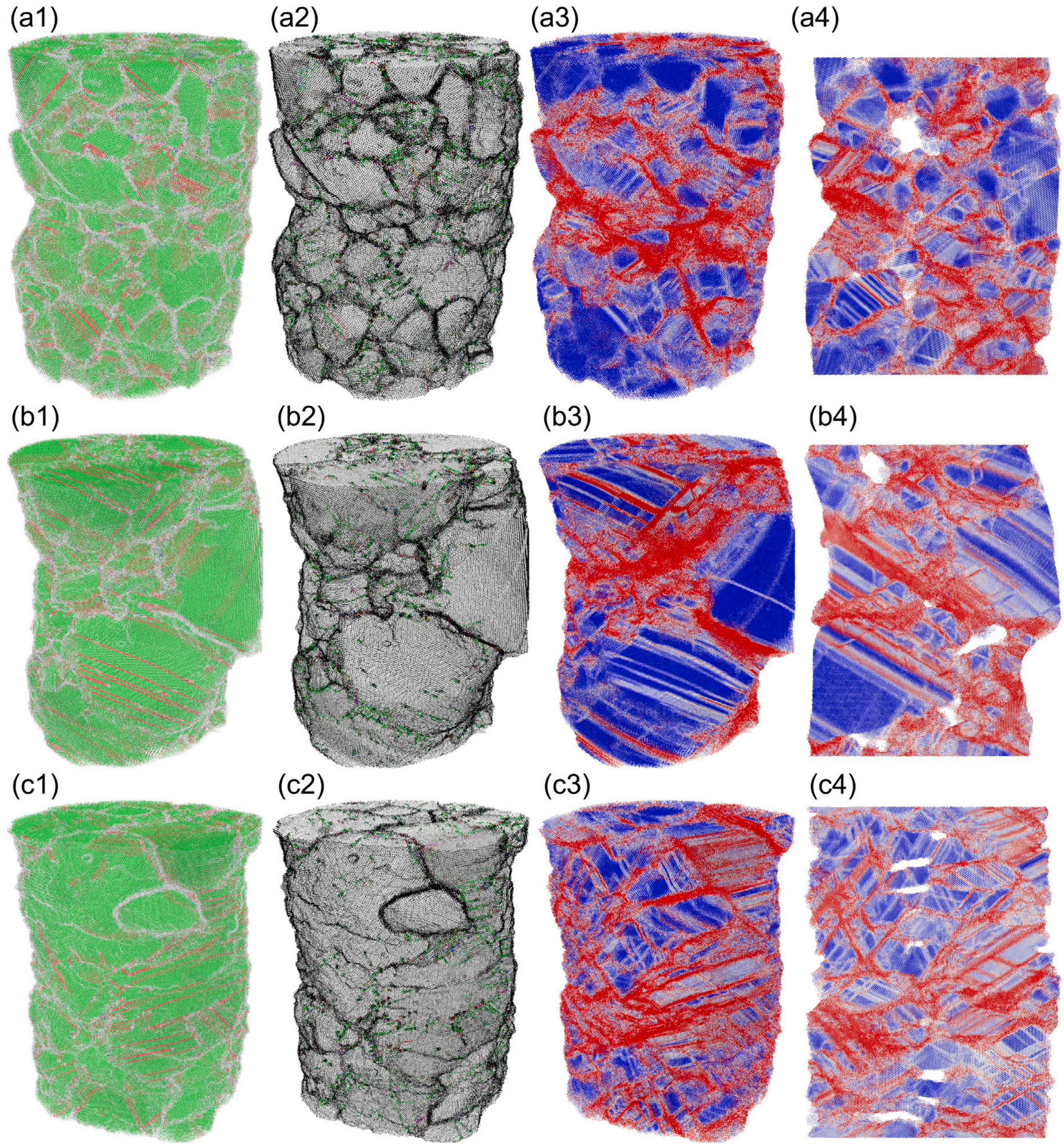

Fig. 8. Post-compression MD simulation results linking particle morphology to dislocation activity and local strain distribution in sintered Cu pillars. (a1–a4) Atomic structure, dislocation distribution, atomic strain distribution, and corresponding cross-sectional strain map of the monomodal structure. (b1–b4) Corresponding results for the bimodal structure. (c1–c4) Corresponding results for the flake-shaped structure.

contacts and mechanical interlocking between high-aspect-ratio flakes, particle-scale rotation is strongly constrained during densification. As a result, initially distorted flake domains are preferentially accommodated by bending, segmentation and constrained fragmentation, which subdivide elongated orientation domains into smaller units [96]. The reduced GROD therefore indicates a transition from diffuse intragranular lattice rotation in the initial flake network to deformation governed by inter-flake constraint, pore-collapse-induced compaction and flake breakage during compression.

3.4. Deformation mechanisms revealed by MD simulations

To complement the experimental observations and to elucidate the deformation mechanisms at the atomic scale, MD simulations were conducted for pillars with monomodal, bimodal and flake-shaped particle structures. The post-compression morphologies are shown in Figs. 8a1–c1. The monomodal pillar maintains a nearly axisymmetric compacted shape, indicating relatively homogeneous deformation. By contrast, the bimodal pillar shows pronounced local distortion caused by the extrusion of coarse particles. The flake-shaped pillar develops dense inclined planar traces aligned with the preferred shear direction. These simulated morphologies are consistent with the experimentally observed deformation modes of the micro-pillars (Figs. 3g–i), confirming the critical role of particle morphology in regulating strain localization during compression. The dislocation configurations reveal distinct morphology-dependent modes of plastic accommodation [97]. In the monomodal structure, dislocations are widely distributed throughout the interparticle regions, particularly near particle contacts and sintered necks, forming a forest-like network (Fig. 8a2) [98]. This feature indicates extensive dislocation interaction at multiple contact-confined deformation sites, enabling distributed plastic flow. In the

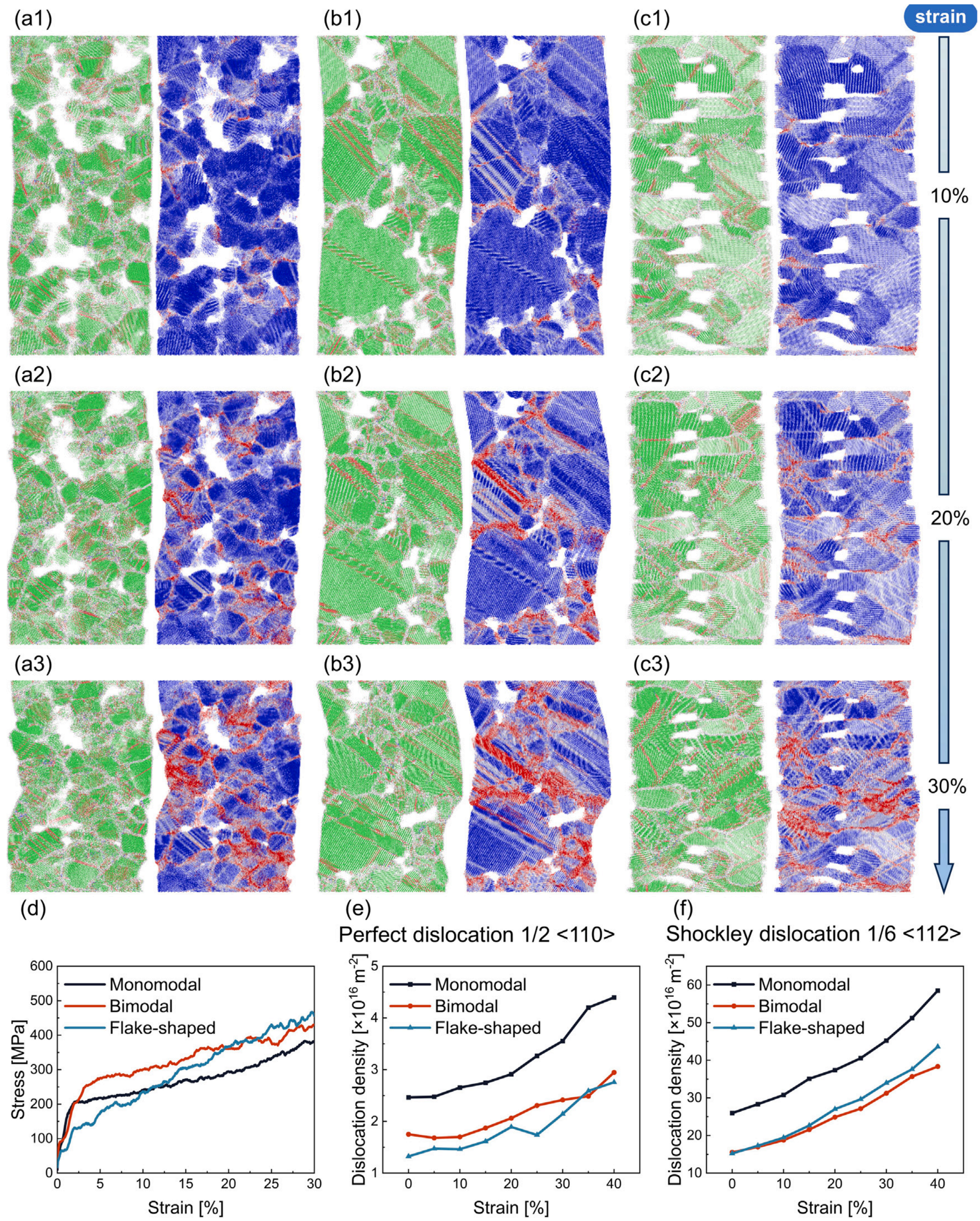

Fig. 9. MD deformation evolution of sintered Cu pillars with different particle morphologies. (a1–a3) Interfacial deformation and dislocation configurations in the monomodal structure at applied compressive strains of 10%, 20%, and 30%, respectively. (b1–b3) Corresponding bimodal structure. (c1–c3) Corresponding flake-shaped structure. (d) Simulated stress–strain responses. (e) Strain-dependent evolution of perfect dislocation density, 1/2⟨110⟩. (f) Strain-dependent evolution of Shockley partial dislocation density, 1/6⟨112⟩.

bimodal structure, dislocations concentrate mainly at coarse/fine particle transition regions (Fig. 8b2), where heterogeneous load transfer and geometric incompatibility produce strong local strain gradients. In the flake-shaped structure, the dislocation arrangement becomes highly directional (Fig. 8c2). Dislocation segments connect along flake interfaces, inter-flake bridges, pore-confined channels and inclined defect traces, forming band- or chain-like dislocation-enriched pathways across large flake domains. This trend agrees with the dislocation structures identified by TKD (Figs. 6, 7). The atomic strain maps further clarify the spatial distribution of plastic deformation. In the monomodal pillar, the strain field is relatively symmetric and broadly distributed, with high-strain regions concentrated along particle boundaries, sintered necks and pore-adjacent areas (Fig. 8a3). The magnified view (Fig. 8a4) shows multiple intersecting shear-band-like zones rather than a single dominant band, suggesting cooperative particle compaction, neck deformation and interparticle shear. In the bimodal pillar, strain localizes preferentially along coarse-particle boundaries and coarse/fine transition regions, forming a dominant shear-band-like path that promotes particle-scale extrusion (Fig. 8b3). The enlarged map (Fig. 8b4) also reveals intraparticle strain bands within coarse particles, indicating that these domains accommodate plastic strain internally while interacting with the surrounding fine-particle matrix [99]. In the flake-shaped pillar, strain localization is strongly controlled by the orientation of flake-derived domains (Fig. 8c3). The magnified strain map (Fig. 8c4) shows that major high-strain bands develop preferentially along interfaces between nearly parallel sintered flake blocks, while secondary intraflake bands indicate local bending, segmentation and fragmentation during compression.

To further elucidate the hierarchical evolution of deformation during compression, Fig. 9 presents the strain-dependent interfacial strain fields, defect configurations and mechanical responses of the three particle structures. The corresponding pillar morphology evolution is provided in Figs. S6-S8. In the monomodal structure, plasticity is initiated at 10% strain by localized high-strain regions and dislocation segments near particle contacts, sintered necks and pore-adjacent interfaces (Fig. 9a1). With increasing strain to 20%, these initially discrete sites expand and interconnect through the interparticle network, accompanied by increased dislocation accumulation (Fig. 9a2). At 30% strain, the strain field develops into a spatially distributed, multi-shear-band-like pattern, indicating progressive percolation of plastic deformation through the connected particle skeleton (Fig. 9a3). Consistently, the monomodal pillar exhibits a clear elastic-to-plastic transition in the simulated stress–strain response and maintains the highest dislocation density throughout compression (Figs. 9d–f). The bimodal structure shows stronger spatial heterogeneity because of the coarse-particle framework. Between 10% and 20% strain, localized deformation develops both within coarse particles and at coarse/fine transition regions, indicating concurrent intraparticle and interfacial plasticity (Figs. 9b1, b2). At 30% strain, these localized regions coalesce into an inclined shear-band-like path guided by the coarse-particle arrangement, accompanied by particle-scale extrusion and pronounced intraparticle strain bands in the coarse domains (Fig. 9b3). The corresponding stress–strain curve also shows a distinct yielding event followed by plastic flow, while the dislocation density remains lower than that of the monomodal structure (Figs. 9d–f).

Morphology-controlled strain partitioning is most evident in the flake-shaped structure. During compression, slightly misoriented flake domains are compacted through extended face-to-face contacts, causing local reorientation and the formation of larger, coherently stacked sintered blocks (Figs. 9c1–c3). By contrast, flake blocks with larger angular mismatch cannot be fully aligned; their interfaces instead become preferential sites for strain localization and evolve into inclined shear-band-like paths. Accordingly, the flake-shaped pillar shows a gradual transition from elastic loading to plastic deformation without a distinct yield point, and its dislocation density remains lower than that of the monomodal pillar (Figs. 9d–f). Across all three structures, both perfect and Shockley dislocations increase with strain, reflecting progressive defect accumulation during compression. In addition, the strain-dependent increase in stair-rod, Hirth and Frank partial dislocations further indicates the accumulation of sessile defects during deformation (Fig. S9). The predominance of Shockley partial dislocations ($1/6\langle 112\rangle$), over perfect dislocations ($1/2\langle 110\rangle$) and other dislocation types, indicates that plasticity is mainly accommodated by partial-dislocation slip and stacking-fault formation under the confined interparticle stress state, while particle morphology further regulates dislocation locking and strain accommodation.

4. Conclusion

This study establishes a morphology-dependent understanding of microstructure evolution, deformation mechanisms and mechanical performance in pressure-assisted sintered Cu particle structures. By combining micro-pillar compression, TEM/TKD characterization and MD simulations, the work clarifies how monomodal, bimodal and flake-shaped particles regulate pore topology, load-transfer pathways and failure modes. The main findings are as follows:

1. Particle morphology strongly regulates the stiffness-strength balance in sintered Cu structures. The monomodal, bimodal and flake-shaped structures exhibit elastic modulus of 12.53 ± 0.72, 7.43 ± 0.27 and 7.84 ± 0.85 GPa, respectively, and yield strengths of 403.01 ± 36.46, 434.11 ± 9.54 and 450.65 ± 65.84 MPa, respectively. This combination of low effective stiffness and high yield strength originates from the porous load-bearing network, where pores reduce elastic modulus, while sintering necks and particle interlocking enhance resistance to plastic instability.

2. Particle morphology defines the load-transfer topology and thereby the dominant deformation mode of the sintered Cu micropillars. The monomodal structure deforms through distributed, nearly axisymmetric compaction of the fine-particle skeleton. The bimodal structure exhibits heterogeneous load partitioning, in which coarse particles carry the primary load and promote localized extrusion. The flake-shaped structure shows anisotropic, geometry-guided deformation, where platelet stacking and inter-flake mismatch redirect load transfer and trigger shear localization.

3. TEM and TKD reveal that morphology also governs grain-scale plastic-strain accommodation. The monomodal structure shows distributed pore collapse, neck deformation and dislocation activity, whereas the bimodal structure concentrates strain gradients and dislocation accumulation near coarse/fine transition regions and within large particles. In the flake-shaped structure, deformation follows lamellar domains and inter-flake boundaries through bending, fragmentation and localized shear. The corresponding post-compression GND densities are 4.36×10^{14} m^{-2}, 3.69×10^{14} m^{-2} and 4.11×10^{14} m^{-2}, with average GROD values of 1.14, 1.51 and 2.52 for the monomodal, bimodal and flake-shaped structures, respectively.

4. MD simulations reproduce the morphology-specific compression modes and provide an atomistic interpretation of the experimental observations. The simulations reveal plastic-strain percolation in the monomodal structure, coarse-particle-guided localization in the bimodal structure and contact-induced flake alignment with inter-block shear in the flake-shaped structure. The dominance of Shockley partial dislocations ($1/6\langle 112\rangle$) indicates partial-dislocation-mediated plasticity under the confined interparticle stress state.

In summary, this study identifies particle morphology as a primary structural variable controlling deformation and mechanical response in sintered porous metals. By linking packing topology, pore structure and contact geometry to load transfer and plastic accommodation, the results provide a mechanistic basis for tuning stiffness, strength and damage tolerance beyond conventional sintering parameters. This morphology-guided design strategy provides practical guidance for selecting Cu powders in electronic packaging by linking particle morphology to the expected compaction, extrusion and shear-localization failure modes of sintered Cu interconnects.

CRediT authorship contribution statement

Tianxing Du: Writing – original draft, Methodology, Investigation. **Chenshan Gao:** Methodology, Investigation. **Olof Bäcke:** Methodology, Investigation. **Lai Wei:** Methodology, Investigation. **Huaiyu Ye:** Supervision, Methodology, Investigation. **Guoqi Zhang:** Supervision. **Magnus Hörnqvist Colliander:** Methodology, Investigation. **Leiming Du:** Writing – review & editing, Supervision, Methodology, Investigation.

Declaration of competing interest

The authors declare that they have no known competing financial interests or personal relationships that could have appeared to influence the work reported in this paper.

Acknowledgments

The authors would like to acknowledge the financial support from the ECSEL Joint Undertaking (JU) under grant agreement No 876659. The JU receives support from the European Union's Horizon 2020 research and innovation program and Germany, Austria, Slovakia, Sweden, Finland, Belgium, Italy, Spain, Netherlands, Slovenia, Greece, France, and Turkey.

Appendix A. Supplementary data

Supplementary material related to this article can be found online at https://doi.org/10.1016/j.msea.2026.150688.

Data availability

Data will be made available on request.

References

[1] N. Takano, K. Fukasawa, K. Nishiyabu, Structural strength prediction for porous titanium based on micro-stress concentration by micro-CT image-based multiscale simulation, Int. J. Mech. Sci. 52 (2) (2010) 229–235.
[2] A. Cherqaoui, F. Copes, C. Paternoster, S. Gélinas, P. Mengucci, C. Blais, D. Mantovani, Effect of powder preparation on degradation behavior and cytotoxicity of sintered porous biodegradable FeMnC alloys for biomedical applications, J. Mater. Sci. Technol. 236 (2025) 198–214.
[3] I.-H. Oh, N. Nomura, N. Masahashi, S. Hanada, Mechanical properties of porous titanium compacts prepared by powder sintering, Scr. Mater. 49 (12) (2003) 1197–1202.
[4] T.Y. Kim, C.Y. Im, J.H. Choi, D. Gu, S. Yoon, U.-H. Kim, S.J. Kim, Fabrication of a porous copper/graphite/zirconium oxide hybrid anode via screen printing for lithium-ion batteries, Adv. Funct. Mater. 34 (51) (2024) 2411648.
[5] C.-J. Bae, C.K. Erdonmez, J.W. Halloran, Y.-M. Chiang, Design of battery electrodes with dual-scale porosity to minimize tortuosity and maximize performance, Adv. Mater. 25 (9) (2012) 1254–1258.
[6] N. Hayashi, K. Watanabe, K. Shimanoe, Co-sintering a cathode material and garnet electrolyte to develop a bulk-type solid-state Li metal battery with wide electrochemical windows, J. Mater. Chem. A 12 (9) (2024) 5269–5281.
[7] A. Sazvar, M. Hajibandeh, P. Vafaei, E. Hosseinzadeh, M. Jabbari, Review of recent progress in sintering of solid-state batteries: Application and modelling, J. Energy Storage 101 (2024) 113863.
[8] H. Chi, L. Xiao, T. Deng, B. Pan, J. Yuan, Modeling and characterization of sintered YSZ/NiO porous electrode structural properties using coarse-graining molecular dynamics method, Ceram. Int. 50 (14) (2024) 26205–26219.
[9] M. Cui, Y. Zhao, B. Zhang, Z. Zhang, X. Shi, J. Lai, K. Shan, S. Wei, H. Pang, Highly efficient Ni3Se2@ sintering porous Ni catalytic electrode for durable hydrogen evolution reaction, Int. J. Hydrog. Energy 76 (2024) 181–189.
[10] K. Shan, Y. Zhao, B. Zhang, S. Wei, J. Lin, J. Ma, H. Pang, Spark plasma sintered porous Ni as a novel substrate of Ni3Se2@Ni self-supporting electrode for ultra-durable hydrogen evolution reaction, J. Colloid Interface Sci. 662 (2024) 31–38.
[11] L. Wang, F. Xia, W. Xu, G. Wang, S. Hong, F. Cheng, B. Wu, N. Zheng, Antioxidant high-conductivity copper pastes based on core–shell copper nanoparticles for flexible printed electronics, Adv. Funct. Mater. 33 (2023) 2215127.
[12] T. Kirscht, A. Bera, M. Marander, C. Grota, F. Liu, S. Jiang, Smaller is better: reducing silver nanoparticle size without excess ligands enhances conductivity and flexibility in printed thin films, Npj Flex. Electron. 9 (2025) 113.
[13] I. Theodorakos, F. Zacharatos, R. Geremia, D. Karnakis, I. Zergioti, Selective laser sintering of Ag nanoparticles ink for applications in flexible electronics, Appl. Surf. Sci. 336 (2015) 157–162.
[14] L. Liu, Q. Wang, S. Robertson, C. Chen, C. Liu, Z. Zhou, C. Tuo, H. Ma, L. Nong, X. Cao, Z. Chen, Study on sintering parameters and bonding mechanism of Cu@Ag preform via electromagnetic compaction for power electronics, J. Alloys Compd. 1030 (2025) 180842.
[15] X. Long, W. Tang, Y. Feng, C. Chang, L.M. Keer, Y. Yao, Strain rate sensitivity of sintered silver nanoparticles using rate-jump indentation, Int. J. Mech. Sci. 140 (2018) 60–67.
[16] W. Liu, X. Wang, J. Zhang, G. Zhang, C. Chen, P. Liu, Quartet structure generation set algorithm based 3D reconstruction on porous structures of sintered copper joints for power electronics packaging, Scr. Mater. 265 (2025) 116750.
[17] X. Yan, L. Du, C. Gu, T. Tian, C. Gao, G. Zhang, J. Fan, Microscale mechanical properties in sintered copper nanoparticles, Mater. Sci. Eng.: A 943 (2025) 148684.
[18] J. Carr, X. Milhet, P. Gadaud, S. Boyer, G.E. Thompson, P. Lee, Quantitative characterization of porosity and determination of elastic modulus for sintered micro-silver joints, J. Mater. Process. Technol. 225 (2015) 19–23.
[19] P. Gadaud, V. Caccuri, D. Bertheau, J. Carr, X. Milhet, Ageing sintered silver: Relationship between tensile behavior, mechanical properties and the nanoporous structure evolution, Mater. Sci. Eng.: A 669 (2016) 379–386.
[20] M. Tang, L. Wang, Z. Xin, Z. Luo, High energy absorption design of porous metals using deep learning, Int. J. Mech. Sci. 282 (2024) 109593.
[21] D. Hu, L. Du, M. Alfreider, J. Fan, D. Kiener, G. Zhang, Microscopic fracture toughness of notched porous sintered Cu micro-cantilevers for power electronics packaging, Mater. Sci. Eng.: A 897 (2024) 146316.
[22] H. Lippmann, R. Iankov, Mathematical modeling of sintering during powder forming processes, Int. J. Mech. Sci. 39 (5) (1997) 585–596.
[23] Y. Zuo, C. Zhao, A. Robador, M. Wickham, S.H. Mannan, Quasi-in-situ observation of the grain growth and grain boundary movement in sintered Cu nanoparticle interconnects, Acta Mater. 236 (2022) 118135.
[24] C. Chen, S. Nagao, K. Suganuma, J. Jiu, T. Sugahara, H. Zhang, T. Iwashige, K. Sugiura, K. Tsuruta, Macroscale and microscale fracture toughness of microporous sintered Ag for applications in power electronic devices, Acta Mater. 129 (2017) 41–51.
[25] X. Shang, Y. Lin, K. Hou, Y. Zhong, C. Cao, Y. Wang, H. Zeng, J. Lin, Effects of spark plasma sintering parameters on sintering mechanism of yttrium hydride, J. Mater. Sci. Technol. 229 (2025) 106–115.
[26] H. Cao, J. Yuan, X. Wu, T. Li, L. Wang, J. Suhr, Z. Zhang, Micron- and nano-sized copper sintering pastes: Materials, processes, and applications, Mater. Des. 256 (2025) 114291.
[27] F. Yu, R.W. Johnson, M.C. Hamilton, Low temperature, fast sintering of micro-scale silver paste for die attach for 300° C applications, Int. Symp. Microelectron. (2015) 000654.
[28] L. Du, K. Liu, D. Hu, O. Bäcke, X. Hu, X. Ji, J. Fan, R.H. Poelma, M.H. Colliander, G. Zhang, Microstructural and mechanical anisotropy in pressure-assisted sintered copper nanoparticles, Acta Mater. 287 (2025) 120772.
[29] V.P. Onbattuvelli, R.K. Enneti, S.V. Atre, The effects of nanoparticle addition on the sintering and properties of bimodal AlN, Ceram. Int. 38 (8) (2012) 6495–6499.
[30] Z. Wang, K. Zhao, J. Liu, L. An, Enhanced mechanical properties of aluminum matrix composite reinforced by bimodal-sized (submicron+ nano) particles, J. Alloys Compd. (2025) 183437.
[31] K. Zhang, Z. Cao, J. Sun, B. Liu, K. Cai, B. Li, C. Fan, Effects of hybrid graphene and SiC nanowire on the mechanical properties of gradient (HfNbTaTiZr)C-based nanocomposites, J. Alloys Compd. 1035 (2025) 181565.
[32] C. Wang, G. Li, L. Xu, J. Li, D. Zhang, T. Zhao, R. Sun, P. Zhu, Low temperature sintered silver nanoflake paste for power device packaging and its anisotropic sintering mechanism, ACS Appl. Electron. Mater. 3 (2021) 5365–5373.
[33] J. Yeom, S. Nagao, C. Chen, T. Sugahara, H. Zhang, C. Choe, C.-F. Li, K. Suganuma, Ag particles for sinter bonding: Flakes or spheres? Appl. Phys. Lett. 114 (2019) 253103.
[34] C. Chen, K. Suganuma, Microstructure and mechanical properties of sintered Ag particles with flake and spherical shape from nano to micro size, Mater. Des. 162 (2019) 311–321.
[35] B. Yang, M. Yu, N. Mollaei, Y. Li, M.A. Monclus, J. Wang, J. Llorca, Deformation mechanisms of pure Zn studied by micropillar compression tests at room and elevated temperatures, Acta Mater. 304 (2026) 121808.
[36] A. Rezaei, N. Mollaei, M. Sarebanzadeh, B. Yang, S.M. Fatemi, J. Llorca, Ascertaining the plastic deformation mechanisms of polycrystalline extruded Zn through in situ SEM/EBSD mechanical tests, Int. J. Plast. 196 (2026) 104548.
[37] G. Saada, T. Kruml, Deformation mechanisms of nanograined metallic polycrystals, Acta Mater. 59 (6) (2011) 2565–2574.
[38] J.J. Wang, N.R. Tao, K. Lu, Revealing the deformation mechanisms of nanograins in gradient nanostructured Cu and CuAl alloys under tension, Acta Mater. 180 (2019) 231–242.
[39] S. Akhondzadeh, M. Kang, R.B. Sills, K.T. Ramesh, W. Cai, Direct comparison between experiments and dislocation dynamics simulations of high rate deformation of single crystal copper, Acta Mater. 250 (2023) 118851.
[40] C.X. Huang, K. Wang, S.D. Wu, Z.F. Zhang, G.Y. Li, S.X. Li, Deformation twinning in polycrystalline copper at room temperature and low strain rate, Acta Mater. 54 (3) (2006) 655–665.
[41] R. Pokharel, J. Lind, S.F. Li, P. Kenesei, R.A. Lebensohn, R.M. Suter, A.D. Rollett, In-situ observation of bulk 3D grain evolution during plastic deformation in polycrystalline Cu, Int. J. Plast. 67 (2015) 217–234.
[42] J. Hu, Y.N. Shi, X. Sauvage, G. Sha, K. Lu, Grain boundary stability governs hardening and softening in extremely fine nanograined metals, Science 355 (6331) (2017) 1292–1296.

[43] T.H. Fang, W.L. Li, N.R. Tao, K. Lu, Revealing extraordinary intrinsic tensile plasticity in gradient nano-grained copper, Science 331 (6024) (2011) 1587–1590.
[44] Y. Fu, V.Y. Mehr, Z. Liu, M.R. Toroghinejad, R. Guo, Enhanced torsional strength and plasticity synergy of multi-component alloy via multi-level gradient structures, Mater. Today Commun. 40 (2024) 110185.
[45] Y. Fu, C. Zhang, W. Liu, Z. Liu, P. Ying, Y. Zhang, Pathway to lead-free brass by stabilizing graphite via tic-β phase interface, J. Mater. Res. Technol. (2026).
[46] L. Du, W. Jiao, O. Backe, M.H. Colliander, R.H. Poelma, J. Fan, W.D. van Driel, X. Fan, G. Zhang, Interface strength and crack propagation mechanisms in sintered copper nanoparticles, Acta Mater. 296 (2025) 121187.
[47] L. Du, G. Schaffar, W. Jiao, K. Liu, R.H. Poelma, V. Maier-Kiener, J. Fan, D. Kiener, W.D. van Driel, X. Fan, G. Zhang, Tailoring microstructure and mechanical properties of sintered Cu nanoparticles, Acta Mater. 300 (2025) 121501.
[48] L. Salvi, B. Smaniotto, F. Hild, M.G. Tarantino, Tensile deformation and failure of AlSi10Mg random cellular metamaterials, Int. J. Mech. Sci. 281 (2024) 109612.
[49] C. Gu, X. Hu, K. Lu, T. Wang, X. Yan, W. Chen, J. Chen, X. Fan, G. Zhang, J. Fan, Revealing thermo-mechanical degradation mechanism of sintered silver nanoparticles under thermal shock via microstructure characterization and kinetic Monte Carlo simulation, Mater. Sci. Eng.: A (2026) 149646.
[50] X. Milhet, A. Nait-Ali, D. Tandiang, Y.J. Liu, D. Van Campen, V. Caccuri, M. Legros, Evolution of the nanoporous microstructure of sintered Ag at high temperature using in-situ X-ray nanotomography, Acta Mater. 156 (2018) 310–317.
[51] L. Du, G. Schaffar, R.H. Poelma, J. Fan, W.D. van Driel, X. Fan, D. Kiener, G. Zhang, V. Maier-Kiener, Strain rate and temperature dependent viscoplasticity of sintered cu nanoparticles, Mater. Des. 256 (2025) 114319.
[52] S. Lee, S.-j. Han, Y. Kim, K.-S. Jang, Copper sintering pastes with various polar solvents and acidic activators, ACS Omega 8 (42) (2023) 39135–39142.
[53] J.C. Petit, M. Sperl, Pressure model and scaling laws in jammed bidisperse granular packings: JC Petit, M. Sperl, Granul. Matter 27 (1) (2025) 23.
[54] R. Hosseinabadi, H. Riesch-Oppermann, J.P. Best, G. Dehm, C. Kirchlechner, Size scaling in bi-crystalline Cu micropillars containing a coherent twin boundary, Acta Mater. 230 (2022) 117841.
[55] Y. Zhang, T.J. Nizolek, L. Capolungo, N. Li, J.S. Carpenter, R.J. McCabe, Strong interfaces: the key to high strength in nano metallic laminates, Acta Mater. 280 (2024) 120298.
[56] T. Vermeij, A. Sharma, D. Steinbach, J. Lou, J. Michler, X. Maeder, In situ transmission Kikuchi diffraction tensile testing, Scr. Mater. 261 (2025) 116608.
[57] P.W. Trimby, Y. Cao, Z. Chen, S. Han, K.J. Hemker, J. Lian, X. Liao, P. Rottmann, S. Samudrala, J. Sun, J.T. Wang, J. Wheeler, J.M. Cairney, Characterizing deformed ultrafine-grained and nanocrystalline materials using transmission Kikuchi diffraction in a scanning electron microscope, Acta Mater. 62 (2014) 69–80.
[58] A.P. Thompson, H.M. Aktulga, R. Berger, D.S. Bolintineanu, W.M. Brown, P.S. Crozier, P.J. in 't Veld, A. Kohlmeyer, S.G. Moore, T.D. Nguyen, R. Shan, M.J. Stevens, J. Tranchida, C. Trott, S.J. Plimpton, LAMMPS - a flexible simulation tool for particle-based materials modeling at the atomic, meso, and continuum scales, Comput. Phys. Comm. 271 (2022) 108171.
[59] A. Stukowski, Visualization and analysis of atomistic simulation data with OVITO–the open visualization tool, Modelling Simul. Mater. Sci. Eng. 18 (2010) 015012.
[60] P.L. Williams, Y. Mishin, J.C. Hamilton, An embedded-atom potential for the Cu–Ag system, Modelling Simul. Mater. Sci. Eng. 14 (2006) 817–833.
[61] S. Ganisetti, A. Atila, J. Guénolé, A. Prakash, J. Horbach, L. Wondraczek, E. Bitzek, The origin of deformation induced topological anisotropy in silica glass, Acta Mater. 257 (2023) 119108.
[62] M. Yu, Y. Cui, J. Wang, Y. Chen, Z. Ding, T. Ying, J. Llorca, X. Zeng, Critical resolved shear stresses for slip and twinning in Mg-Y-Ca alloys and their effect on the ductility, Int. J. Plast. 162 (2023) 103525.
[63] H. Bei, S. Shim, G.M. Pharr, E.P. George, Effects of pre-strain on the compressive stress–strain response of Mo-alloy single-crystal micropillars, Acta Mater. 56 (2008) 4762–4770.
[64] P.J. Imrich, C. Kirchlechner, C. Motz, G. Dehm, Differences in deformation behavior of bicrystalline Cu micropillars containing a twin boundary or a large-angle grain boundary, Acta Mater. 73 (2014) 240–250.
[65] J.A. Sharon, K. Hattar, B.L. Boyce, L.N. Brewer, Compressive properties of $\langle 110 \rangle$ Cu micro-pillars after high-dose self-ion irradiation, Mater. Res. Lett. 2 (2) (2014) 57–62.
[66] M.K. Bhat, P.T. Sukumar, L. Langenohl, J.P. Best, G. Dehm, Role of Ag segregation on microscale strengthening and slip transmission in an asymmetric $\Sigma 5$ copper grain boundary, Acta Mater. 255 (2023) 119081.
[67] N.V. Malyar, J.S. Micha, G. Dehm, C. Kirchlechner, Size effect in bi-crystalline micropillars with a penetrable high angle grain boundary, Acta Mater. 129 (2017) 312–320.
[68] X. Hou, S. Krauß, B. Merle, Additional grain boundary strengthening in length-scale architectured copper with ultrafine and coarse domains, Scr. Mater. 165 (2019) 55–59.
[69] C. Howard, D. Frazer, A. Lupinacci, S. Parker, R.Z. Valiev, C. Shin, B.W. Choi, P. Hosemann, Investigation of specimen size effects by in-situ microcompression of equal channel angular pressed copper, Mater. Sci. Eng.: A 649 (2016) 104–113.
[70] R. Ramachandramoorthy, S. Kalácska, G. Poras, J. Schwiedrzik, T.E.J. Edwards, X. Maeder, T. Merle, G. Ercolano, W.W. Koelmans, J. Michler, Anomalous high strain rate compressive behavior of additively manufactured copper micropillars, Appl. Mater. Today 27 (2022) 101415.
[71] N.L. Okamoto, D. Kashioka, T. Hirato, H. Inui, Specimen- and grain-size dependence of compression deformation behavior in nanocrystalline copper, Int. J. Plast. 56 (2014) 173–183.
[72] A. Khalajhedayati, Z. Pan, T.J. Rupert, Manipulating the interfacial structure of nanomaterials to achieve a unique combination of strength and ductility, Nat. Commun. 7 (2016) 10802.
[73] L. Lu, X. Chen, X. Huang, K. Lu, Revealing the maximum strength in nanotwinned copper, Science 323 (5914) (2009) 607–610.
[74] M. Zhang, Z. Rao, T. Xu, L. Fang, Quantifying the influence of grain boundary activities on hall-petch relation in nanocrystalline cu by using phase field and atomistic simulations, Int. J. Plast. 135 (2020) 102846.
[75] N. Khiara, M. Coulombier, J.-P. Raskin, Y. Bréchet, T. Pardoen, F. Onimus, Helium nano-bubbles in copper thin films slows down creep under ion irradiation, Acta Mater. 288 (2025) 120854.
[76] Y. Li, Y. Wei, X. Luo, C. Li, N. Ma, Correlating particle impact condition with microstructure and properties of the cold-sprayed metallic deposits, J. Mater. Sci. Technol. 40 (2020) 185–195.
[77] D. Kiener, P.J. Guruprasad, S.M. Keralavarma, G. Dehm, A.A. Benzerga, Work hardening in micropillar compression: In situ experiments and modeling, Acta Mater. 59 (2011) 3825–3840.
[78] L. Meng, P. Lu, S. Li, Packing properties of binary mixtures in disordered sphere systems, Particuology 16 (2014) 155–166.
[79] J.C. Petit, M. Sperl, Additional jamming transition in two-dimensional bidisperse granular packings, Phys. Rev. Res. 7 (2025) L022073.
[80] M. Buttard, B. Chéhab, C. Josserond, F. Charlot, P. Lhuissier, X. Bataillon, A. Deschamps, J. Villanova, M. Fivel, J.-J. Blandin, G. Martin, Influence of microstructure heterogeneity on the tensile response of an Aluminium alloy designed for laser powder bed fusion, Acta Mater. 269 (2024) 119786.
[81] J. Wiącek, Geometrical parameters of binary granular mixtures with size ratio and volume fraction: experiments and DEM simulations, Granul. Matter 18 (2016) 42.
[82] J.P. de Bono, G. McDowell, Modelling the mechanical behaviour of clay using particle-scale simulations, Granul. Matter 26 (2024) 29.
[83] U. Ali, M. Kikumoto, Role of particle shape in sheared granular media: roundness and elongation, Powder Technol. 449 (2025) 120436.
[84] A.S. Brandvold, A.C.C. Trindade, W.M. Kriven, Effect of high surface area alumina platelets on squeeze flow properties of geopolymer pastes, Int. J. Appl. Ceram. Technol. 22 (2025) e15095.
[85] H. Fan, Q. Wang, J.A. El-Awady, D. Raabe, M. Zaiser, Strain rate dependency of dislocation plasticity, Nat. Commun. 12 (2021) 1845.
[86] A.L. Greer, Y.Q. Cheng, E. Ma, Shear bands in metallic glasses, Mater. Sci. Eng. R: Rep. 74 (4) (2013) 71–132.
[87] M. Thieme, K.-P. Wieters, F. Bergner, D. Scharnweber, H. Worch, J. Ndop, T.J. Kim, W. Grill, Titanium powder sintering for preparation of a porous functionally graded material destined for orthopaedic implants, J. Mater. Sci., Mater. Med. 12 (2001) 225–231.
[88] S. Meille, M. Lombardi, J. Chevalier, L. Montanaro, Mechanical properties of porous ceramics in compression: On the transition between elastic, brittle, and cellular behavior, J. Eur. Ceram. Soc. 32 (15) (2012) 3959–3967.
[89] L. Yang, J. Bansemer, P. Zaslansky, O. Görke, C. Fleck, Insights into freeze-cast hierarchical water–glass foams via in situ time-lapse phase-contrast enhanced microcomputed tomography: Correlating composition, microstructure, and compression failure, Mater. Des. 246 (2024) 113354.
[90] B. Yang, X. Xu, D. Lunt, F. Zhang, M.D. Atkinson, Y. Li, J. Llorca, X. Zhou, Grain size dependence of microscopic strain distribution in a high entropy alloy at the onset of plastic deformation, Acta Mater. 285 (2025) 120682.
[91] F. Duan, Q. Li, Z. Jiang, L. Zhou, J. Luan, Z. Shen, W. Zhou, S. Zhang, J. Pan, X. Zhou, T. Yang, J. Lu, An order-disorder core-shell strategy for enhanced work-hardening capability and ductility in nanostructured alloys, Nat. Commun. 15 (2024) 6832.
[92] T.H. Chou, W.P. Li, H.W. Chang, X.H. Du, W.S. Chuang, T. Yang, Y.T. Zhu, J.C. Huang, Quantitative analysis of hetero-deformation induced strengthening in heterogeneous grain structure, Int. J. Plast. 159 (2022) 103482.
[93] Y. Li, H. Zhang, X. Shang, M. Liu, S. Zhao, Z. Cui, A multiscale investigation on the preferential deformation mechanism of coarse grains in the mixed-grain structure of 316LN steel, Int. J. Plast. 152 (2022) 103244.
[94] V. Vilchez, S. Rawson, S. Zhou, J. McGregor, M. Lawson, A. Rack, Y. Chen, P.J. Withers, F. Bouville, Effect of grain morphology and interface on the toughness of nacre-like aluminas, Acta Mater. 280 (2024) 120338.
[95] B. Sadeghi, P. Cavaliere, M. Balog, C.I. Pruncu, A. Shabani, Microstructure dependent dislocation density evolution in micro-macro rolled Al2O3/Al laminated composite, Mater. Sci. Eng.: A 830 (2022) 142317.

[96] S. Hao, Q. Fu, L. Meng, F. Xu, J. Yang, A biomimetic laminated strategy enabled strain-interference free and durable flexible thermistor electronics, Nat. Commun. 13 (2022) 6472.
[97] M. Zhang, K. Sun, L. Fang, Influence of grain boundary activites on elastic and plastic deformation of nanocrystalline cu as studied by phase filed and atomistic simulaiton, Int. J. Mech. Sci. 187 (2020) 105911.
[98] C. Zhang, W. Peng, Y. Shao, O. Moliar, L. Lu, X. Zhang, Study on the melting and sintering behavior of Cu-Fe mixed nanoparticles based on molecular dynamics simulations, Mater. Des. 248 (2024) 113457.
[99] R. Zhang, Z. Xu, L. Peng, X. Lai, M.W. Fu, Intragranularly misoriented grain boundary evolution affected by local constraints and grain size in micro-scale deformation of ultra-thin metallic sheets, Int. J. Plast. 157 (2022) 103377.